minerals

MDPI

Article

Clay/Fly Ash Bricks Evaluated in Terms of Kaolin and Vermiculite Precursors of Mullite and Forsterite, and Photocatalytic Decomposition of the Methanol–Water Mixture

Marta Valášková [1,*], Veronika Blahůšková [1], Miroslava Filip Edelmannová [1], Lenka Matějová [1], Karel Soukup [2] and Eva Plevová [3]

[1] Institute of Environmental Technology, CEET, VSB-Technical University of Ostrava, 17. Listopadu 2172/15, 708 00 Ostrava, Czech Republic; veronika.blahuskova@vsb.cz (V.B.); miroslava.filip.edelmannova@vsb.cz (M.F.E.); lenka.matejova@vsb.cz (L.M.)
[2] Institute of Chemical Process Fundamentals of the CAS, Rozvojova 135, 165 02 Prague, Czech Republic; soukup@icpf.cas.cz
[3] Institute of Geonics of the CAS, Studentska 1768, 708 00 Ostrava, Czech Republic; eva.plevova@ugn.cas.cz
* Correspondence: marta.valaskova@vsb.cz; Tel.: +420-597-327-308

Abstract: This study focused on mullite-based and forsterite-based ceramic bricks fired at 1000 °C from mixtures of fly ash (40 mass%) and kaolins or vermiculites (60 mass%). The structural, physical, and mechanical properties were characterized by X-ray powder diffraction, nitrogen physisorption, mercury porosimetry, thermogravimetry, and compressive strength. In the development of green-material-derived photocatalysts, we evaluated fly ash ceramic bricks based on kaolins and vermiculites, which deserve deeper research. Alkali potassium in the mixtures positively influenced the reduction of the firing temperature, shrinkage, small porosity, and high compressive strength of ceramic bricks. The crystallization of mullite in fly ash was observed on exotherm maxima from 813 to 1025 °C. Muscovite/illite admixture in kaolins precursor of mullite-based ceramics reduced the crystallization temperature of mullite by up to 70 °C. Vermiculite–hydrobiotite–phlogopite in mixed layers of a raw vermiculite precursor of forsterite-based ceramics controlled the formation of enstatite and forsterite in the temperature range from 736 ± 6 °C to 827 ± 6 °C. Mullite- and forsterite-based ceramic bricks were also investigated for photocatalytic hydrogen production. The photocatalytic generation of hydrogen in the presence of mullite-based ceramic bricks was positively correlated with the percentages of Fe_2O_3 in the lattice of mullites and in the presence of forsterite-based ceramics with the presence of diopside. Mullite-based ceramic produced the highest yield of hydrogen (320 μmol/g_{cat} after 4 h of irradiation) in the presence of mullite with the highest 10.4% substitution of Fe_2O_3 in the lattice. The forsterite-based ceramic produced the highest hydrogen yields (354 μmol/g_{cat} after 4 h of irradiation) over more active diopside than forsterite.

Keywords: clays; fly ash; kaolin mullite precursor; vermiculite forsterite precursor; firing; compressive strength; photocatalytic capability

check for updates

Citation: Valášková, M.; Blahůšková, V.; Edelmannová, M.F.; Matějová, L.; Soukup, K.; Plevová, E. Clay/Fly Ash Bricks Evaluated in Terms of Kaolin and Vermiculite Precursors of Mullite and Forsterite, and Photocatalytic Decomposition of the Methanol–Water Mixture. *Minerals* **2023**, *13*, 1114. https://doi.org/10.3390/min13091114

Academic Editor: Francisco Franco

Received: 2 July 2023
Revised: 12 August 2023
Accepted: 21 August 2023
Published: 23 August 2023

Copyright: © 2023 by the authors. Licensee MDPI, Basel, Switzerland. This article is an open access article distributed under the terms and conditions of the Creative Commons Attribution (CC BY) license (https://creativecommons.org/licenses/by/4.0/).

1. Introduction

Clay minerals in clay deposits are accompanied by other rock-forming minerals that have a great influence on the final properties of fired clay bricks. Clay bricks have been used for the construction of buildings continuously because of their thermal, physical, and mechanical properties and simple manufacturing process. Fly ashes (FAs) are potentially valuable sources of oxides of silica (SiO_2), alumina (Al_2O_3), and iron oxide (Fe_2O_3) for the manufacture of fired clay masonry bricks [1]. Other oxides in FAs are CaO, MgO, K_2O, and Na_2O, as well as some toxic metals (including As, Pb, Cd, and Ni) in varying amounts. The main crystalline phases are mullite ($3Al_2O_3 \cdot SiO_2$) and quartz. The amount of solid

waste added to clays considering the quality of the products is normally less than 30% by weight [2,3]. Bricks from clay and fly ash in mass ratio up to 80% fired at 1050 °C reached the compressive strength of 25 MPa [4]. A fly-ash-positive effect was found in the reduction of firing shrinkage and a decrease in bulk density [5].

The international classification of bricks is based on different specifications and international standard codes depending on the importance of structures and specific use [6]. Bricks are generally characterized by both interaction with water and mechanical resistance compressive strength. From the manufacturer's point of view, after the clay is dried at above 105 °C, the reduction in size in length or volume is closely related to particle size determined as drying shrinkage (DS). Changes in parameters at firing temperatures in the range of 900–1100 °C are characterized as linear shrinkage (LS), bulk density (BD), and weight loss (WL) [7]. Kaolin clays used in the bricks should contain percentages of SiO_2 in the range between 50% and 60%, Fe_2O_3 not exceeding 10%, and Al_2O_3 in the range between 10% and 20% [7]. Al_2O_3 contributes to the transformation into mullite during firing and to the increase in mechanical resistance [7]. Fly ash (40 mass%) and plastic clay (60 mass%) mixtures were fired between 900 and 1200 °C to the ceramic building materials, including fired clay as building masonry bricks [8]. Kaolin in flay ash mixtures prevented the formation of open pores during mullite sintering [9]. Generally, kaolinite ($Al_4(OH)_8{\cdot}SiO_4O_{10}$) in kaolins in temperatures above 450 °C undergoes dehydroxylation to form metakaolinite ($Al_2SiO_2O_7$). Metakaolinite is converted into Al-Si spinel and amorphous silica around 950 °C. According to the literature, mullites nucleate and crystallize around 1000 °C, depending on the type of precursor, particle size, and heat treatment [10]. Metakaolin additive reduces pores and makes the ceramic waterproof, significantly reducing shrinkage, but increasing the mechanical strengths [11].

Raw vermiculites have recently been used as an inorganic pore-forming additive for the production of porous and lightweight clay bricks [12,13]. Vermiculite is a product of weathering or hydrothermal alteration of hydrobiotite or phlogopite. In the mixed layer structure of raw vermiculite, potassium occupies the interlayer of phlogopite, whereas hydrated cations balancing a net layer charge occupy the interlayer of hydrobiotite and the vermiculite mineral. The hydration state of vermiculite is defined by the 0, 1, or 2 water layers in the interlayer space, or the water layer hydration state (0-, 1-, or 2-WLHS) of the corresponding phases [14]. The hydration state of phlogopite and Mg-vermiculite corresponds to the 2-WLHS and 0-WLHS, respectively. The hydrobiotite is diffracted in the broad band (13.6–11.0 Å) due to the different stacking sequence of Mg-vermiculite and K-biotite [15]. At temperatures around 550 °C, vermiculite and hydrobiotite dehydrate to the 10 Å phase (0-WLHS). The high temperature phases show considerable variation, depending on the interlayer ions and lattice substitutions [16]. At 1000 °C, Mg-vermiculite transforms to enstatite ($Mg_2Si_2O_6$) [17], while the vermiculite–hydrobiotite–phlogopite mixed layer structure transforms to forsterite (Mg_2SiO_4) and leucitelinebreak ($KAlSi_2O_6$) [18,19].

A comprehensive overview [20] summarizes recent advances in the utilization of natural materials (clay mineral and pumice) and waste materials (ash and foundry sand)-based metal oxide photocatalysts for the photodegradation of various pollutants. Silicate glass ceramics belong to the surface-active category, having the unique ability to form strong bonding with metal oxides. Larnite (Ca_2SiO_4) and forsterite (Mg_2SiO_4) degraded methylene blue dye under natural daylight (Sunlight) within the 90 min by 67.2 and 47.1%, respectively [21]. Similarly, the photocatalytic experiment with larnite and forsterite silicate ceramics with rhodamine B (RhB) dye for 120 min confirmed dye degradation of 87% and 79%, respectively [22].

The main aim of this work was the utilization of a kaolin–fly ash mixture into mullite-based ceramic bricks in comparison with the unconventionally used vermiculite–fly ash mixtures into forsterite-based ceramic bricks. Two objectives are focused on in terms of the evaluation of the ceramic bricks: (1) structural, physical, and mechanical properties, and (2) photocatalytic activity performed on the decomposition of the methanol–water mixture.

2. Materials and Methods

2.1. Materials

Fly ash (denoted FA) was obtained from the combustion of black coal captured on an electrostatic precipitator in the powder station (Czech Republic). Clays for the fly ash mixtures were kaolins (samples denoted Ka and Kb), supplied by LB Minerals, Ltd. (Horní Bříza, Czech Republic); metakaolin (sample denoted Mk), supplied by the KERAMOST, Plc. (Most, Czech Republic) under the trade name "thermally processed washed kaolin"; and vermiculites from the Palabora region of South Africa (sample denoted Va) and the Paraiba region of Brazil (sample denoted Vb), supplied by Grena Co. (Veselí nad Lužnicí, Czech Republic).

2.2. Production of Brick Cubes

Kaolins, vermiculites, and fly ash were pulverized by grinding in a PULVERISETTE 6 mill (Fritsch GmbH, Idar-Oberstein, Germany) and sieved to the size fraction under 63 μm.

Dry mixtures of FA (40 mass%) and kaolins or vermiculites (60 mass%) prepared to the ceramic building bricks [8] were homogenized in a bottle at 40 rpm for 1 h (Heidolph MR Hei-Tec, Heidolph, Heidolph Instruments GmbH and Co., KG, Schwabach, Germany) and marked as FA/Ka, FA/Kb, FA/Mk, FA/Va, and FA/Vb. Finally, the homogenized mixtures were milled at 300 rpm for 15 min and prepared for the clay slurry of fine particles containing about 20 mass% distilled water. The slurry was kneaded by hand and formed in the molds of a size of 20 mm × 20 mm × 20 mm. The mols were covered with wet burlap and left to rest overnight. Samples in the molds were dried at 105 °C for 5 h. Dry cubes were taken out of the mold and dried until the weight became constant. Cubes were sintered in a muffle furnace (NABERTHERM L9/11/SW, Nabertherm GmbH, Lilienthal, Germany) at the heating ramp 10 °C/min to the desired temperature of 1000 °C, maintained at this temperature for 2 h, and then slowly cooled to room temperature.

2.3. Characterization Techniques

The chemical composition of fly ash, kaolins, and vermiculites was determined by X-ray fluorescence (XRF) using a SPECTRO XEPOS energy-dispersive X-ray fluorescence (ED-XRF) spectrometer (Spectro Analytical Instruments, Kleve, Germany). The samples (2 × 4 g) were mixed with the wax (0.9 g) and prepared for the pellets by manual hydraulic pressing at 10 tons. The total concentration of Fe was related to Fe_2O_3. The content of Fe(II) was subtracted from the total Fe when it was determined using titration with a 0.1 M solution of $K_2Cr_2O_7$ in a sample decomposed in HCl and HF in a CO_2 atmosphere.

X-ray powder diffraction (XRD) analysis of mineral phases was performed using the Rigaku SmartLab diffractometer (Rigaku Corporation, Tokyo, Japan) under CoKα radiation at 40 kV and 40 mA. The XRD patterns were evaluated using PDXL2 software no. 2.4.2.0 (Rigaku Corporation, Tokyo, Japan) and compared with the database PDF-2, 2015 (ICDD, Newton Square, PA, USA). Lattice parameters of mullites were calculated using Rietveld refinement by PDXL2 software.

Thermogravimetry and differential thermal curves (TG/DTA) were obtained using the thermal analyzer Setsys 24 Evolution (Setaram, Caluire, France), equipped with the thermocouple Pt-Pt90/Rh10. Clays and fly ash mixtures (about 25 mg) loose packed in a crucible were heated to the final temperature 1100 °C at the heating rate 10 °C/min (atmosphere Ar, reference material Al_2O_3).

Determination of mesopore- and macropore-size distribution; specific intrusion volume; V_{intr}; apparent (mercury) density; ρ_{Hg}; and porosity, ε, of solids were realized with the aid of a high-pressure mercury porosimeter, AutoPore IV 9500 (Micromeritics, Norcross, GA, USA). Complementary information about the skeletal (true) density, ρ_{He}, of solids was obtained by using an AccuPyc II 1340 helium pycnometer (Micromeritics, Norcross, GA, USA). Before both analyses, the solids were dried in an oven at 110 °C for several days to remove physisorbed moisture.

The specific surface area (S_{BET}) and the net pore volume (V_{net}) of solids were realized by using nitrogen physisorption at 77 K, performed using a 3Flex volumetric apparatus (Micromeritics, Norcross, GA, USA). Before physisorption analysis, the solids were degassed at a pressure of ≈0.6 bar for 12 h at least at 350 °C to remove the physisorbed water. The specific surface area, S_{BET}, was calculated according to classical BET theory for the p/p_0 range = 0.05–0.25, and net pore volume, V_{net}, was calculated from the adsorption branch of the measured nitrogen adsorption–desorption isotherm at $p/p_0 = 0.99$.

2.4. Testing Procedures of Cube Bricks

2.4.1. Physical and Mechanical Tests

Some physical average values of the five brick cubes of each sample were calculated by Equations (1)–(3) [23]:

$$\text{Mass Loss, WL (\%)} = (WL_{dry} - WL_{fired}/WL_{fired}) \times 100 \quad (1)$$

$$\text{Drying Shrinkage, DS (\%)} = (l_{plastic} - l_{dry}/l_{dry}) \times 100 \quad (2)$$

$$\text{Firing Shrinkage, FS (\%)} = (l_{dry} - l_{fired}/l_{fired}) \times 100 \quad (3)$$

$l_{plastic}$: width, height, and length of the clay brick samples in the plastic state.
l_{dry}: width, height, and length of the clay brick samples in the oven-dry state at 105 °C.
l_{fired}: width, height, and length of the clay brick samples after being fired at 1000 °C.
W_{dry}: mass of the clay brick samples in the oven-dry state at 105 °C.
W_{fired}: mass of the clay brick samples after being fired at 1000 °C.

Compressive strength (CS) was determined on the press machine (BRIO, Hranice, Czech Republic) at a loading rate of 500 N/s. The highest and lowest MPa values were excluded, and the remaining measurements were averaged.

2.4.2. Photocatalytic Activity Test of Bricks

Photocatalytic tests were performed in a home-made photoreactor (stainless steel, volume 305 mL, 8W Hg lamp peak intensity at 254 nm wavelength; Ultra-Violet Products Inc., Upland, CA, USA). Reaction of the methanol–water mixture (100 mL of 50% methanol) with a photocatalyst (0.1 g) was saturated by helium in order to purge the air from the solution. The gaseous products were analyzed by a gas chromatograph (Shimadzu Tracera GC-2010Plus, Shimadzu, Kyoto, Japan) equipped with a BID (barrier discharge ionization detector). All experiments were repeated at least 3 times, and similar results were calculated for the mean values.

3. Results and Discussion

3.1. Chemistry and Phases of Clays, FA, and FA/Clay Ceramic Bricks

The concentrations of elements (from XRF analysis) were converted to the concentrations of stoichiometric oxides (mass%) (Table 1). FA met the requirements SiO_2 + Al_2O_3 + Fe_2O_3 ≥70% to a class F fly ash set forth in ASTM C618-19 [24]. Clays used for brick production should have SiO_2 in the range of 50%–60% and Al_2O_3 in the range of 10%–20% [6]. Manufacturers recommend not exceeding 10% of Fe_2O_3 and 6% of CaO [7]. In this work, the kaolins Ka, Kb, and Mk had SiO_2 in the range from 49 to 58 mass%, while Al_2O_3 exceeded this range by about 15%. Vermiculites Va and Vb had SiO_2 about 5% lower outside this range and Al_2O_3 in the desired range.

In this work, the kaolins Ka, Kb, and Mk had SiO_2 in the range from 49 to 58 mass%, while Al_2O_3 exceeded this range by about 15%. Vermiculites Va and Vb had SiO_2 about 5% lower outside this range and Al_2O_3 in the desired range.

Table 1. Bulk chemical analysis of the major oxide elements (mass%) of the fly ash (FA), kaolins (Ka, Kb, and Mk), and vermiculites (Va and Vb), as well as the FA/clay ceramic bricks (normalized to 100%).

Sample	SiO_2 (mass%)	TiO_2 (mass%)	Al_2O_3 (mass%)	Fe_2O_3 FeO (mass%)	CaO (mass%)	MgO (mass%)	K_2O (mass%)	Na_2O (mass%)	L.O.I [1] (mass%)
FA	53.57	1.21	24.20	7.40	3.36	1.28	2.87	0.81	5.2
Ka	51.35	0.75	31.60	0.71	0.26	0.28	1.40	<0.01	13.30
Kb	49.40	0.87	34.37	0.85	0.19	0.31	2.55	<0.01	10.62
Mk	57.58	0.59	37.08	0.94	0.04	0.28	0.97	<0.01	3.22
Va	43.39	1.11	8.88	5.06	1.43	23.48	4.81	0.15	8.38
Vb	44.02	0.75	11.02	6.65	1.30	23.23	1.82	0.35	9.73
FA	54.90	1.12	28.43	6.65	3.25	2.30	2.95	0.40	n.d. [2]
FA/Ka	56.47	1.02	33.17	3.21	1.27	0.70	2.11	2.05	n.d. [2]
FA/Kb	56.63	0.95	32.18	3.35	1.43	0.77	2.77	1.92	n.d. [2]
FA/Mk	56.54	0.79	36.11	3.08	1.20	0.58	1.70	<0.01	n.d. [2]
FA/Va	46.66	1.14	16.50	8.53	5.22	17.83	4.12	<0.01	n.d. [2]
FA/Vb	47.82	1.09	17.05	7.92	5.58	16.94	3.60	<0.01	n.d. [2]

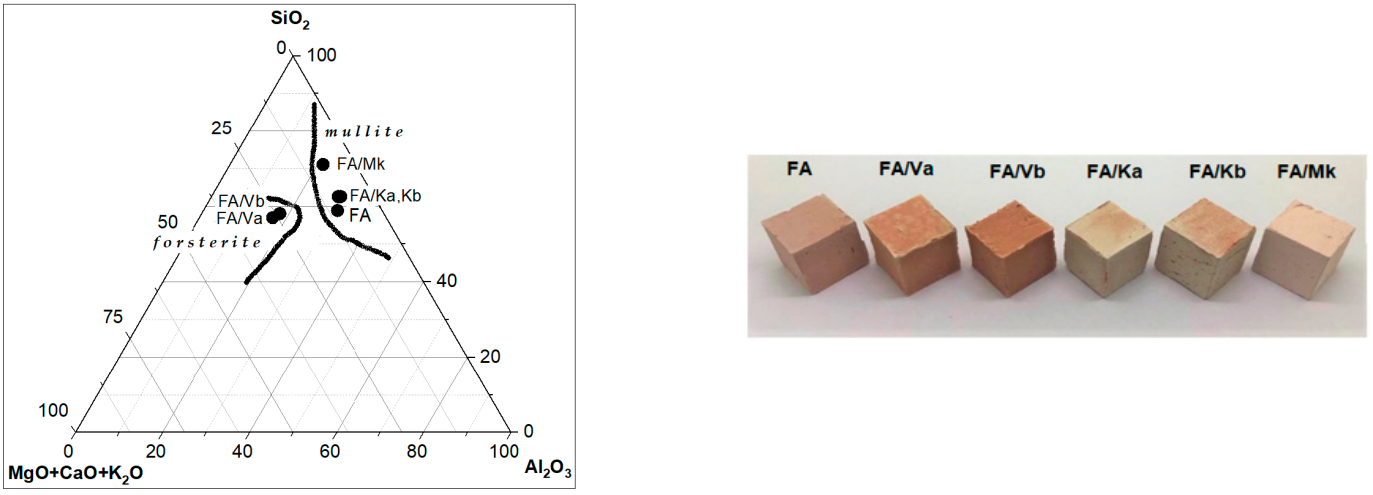
[1] L.O.I. (loss on ignition) at 1000 °C; [2] n.d. (not determined).

Firing temperature highly influences brick properties and is one of the main factors in energy consumption. Although some reviewed works relate higher temperatures (above 1100 °C), these temperatures are infrequently used in the brick industry [25].

XRD phase analysis of kaolins and vermiculites have previously been published [26,27]. FA proved mullite (JCPDS card no. 00-079-1455), quartz (JCPDS card no. 03-065-0466), anorthite (JCPDS card no. 00-076-0948), and hematite (JCPDS card no. 00-089-0596). XRF analysis of FA showed CaO having 3.29 mass% and K_2O having 3.54 mass% (Table 1), observed not only in crystalline phases, and therefore their presence in amorphous and weakly diffracting material was assumed. Kaolin samples Ka and Kb were composed of kaolinite ((JCPDF card no. 00-058-2005), muscovite (JCPDF card no. 01-076-0928), quartz (JCPDF card no. 01-086-2237), and orthoclase (JCPDS card no. 01-076-0824); more details are found in [26]. The metakaolin (Mk) sample was composed of kaolinite (JCPDF card no. 00-058-2028) and illite (JCPDF card no. 00-058-2016)/muscovite (JCPDF card no. 01-076-0928). Vermiculite (Va) contained hydrobiotite (JCPDF card no. 00-049-1057) predominating over vermiculite (JCPDF card no. 00-076-0847), a minority of phlogopite (JCPDF card no. 01–082-2699), and hydroxyapatite (JCPDS card no. 00-064-0738) impurity from the parent rocks. Vermiculite (Vb) is composed of vermiculite (JCPDF card no. 00-076-0847), prevailing slightly over hydrobiotite (JCPDF card no. 00-049-1057), a minority of phlogopite (JCPDF card no. 01–082-2699,) and the accessory minerals tremolite (JCPDF card no. 00-009-0437) and rutile (JCPDF card no. 00-034-0180)); more details can be found in [27].

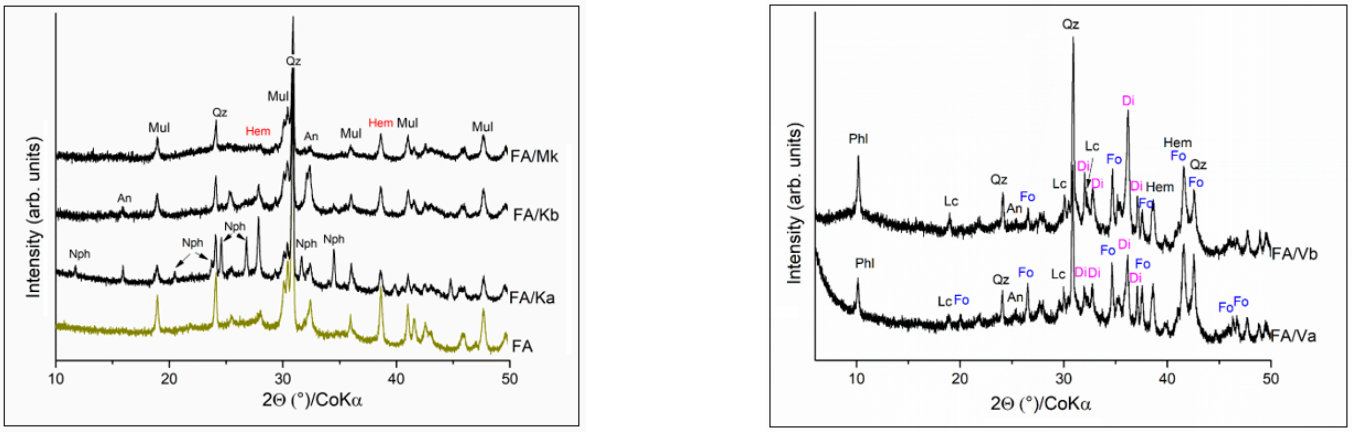
Oxides in FA/clay mixtures when plotted in a ternary diagram of a SiO_2–Al_2O–(MgO + CaO + K_2O) system fall into the areas of mullite and enstatite–forsterite [28] (Figure 1a) in fired ceramic bricks (Figure 1b).

Dry powder FA/clay mixtures were fired at 1000 °C for the mullite-based and forsterite-based ceramics (Figure 2). Crystalline phases in FA/Mk, FA/Ka, and FA/Kb mullite-based bricks (Figure 2a) were mullite (JCPDF card no. 01-079-1455), quartz (JCPDF card no. 01-086-2237), anorthite (JCPDS card no. 01-071-0748), nepheline (JCPDS card no. 01-083-2279), and hematite (JCPDF card no. 01-089-0596).



(**a**) (**b**)

Figure 1. FA/clay mixtures of the ceramic bricks: (**a**) ternary phase diagram of SiO_2–Al_2O–(MgO + CaO + K_2O) of the FA and FA/clay mixtures with the delineation of the chemistry of mullite and forsterite; (**b**) photograph of the fired ceramic brick cubes.



(**a**) (**b**)

Figure 2. X-ray diffraction patterns (segments) of (**a**) mullite-based bricks and (**b**) forsterite-based bricks. An = anorthite; Di = diopside; Fo = forsterite; Hem = hematite; Lc = leucite; Mul = mullite; Nph = nepheline; Phl = phlogopite; Qz = quartz (symbols according to [29]).

Forsterite-based FA/Va and FA/Vb bricks (Figure 2b) are composed of forsterite (JCPDS card no. 00-034-0189), diopside (JCPDS card no. 01-076-6317), leucite (JCPDS card no. 01-076-8735, quartz (JCPDS card no. 01-089-8936), hematite (JCPDS card no. 01-089-8936), anorthite (JCPDS card no. 01-071-0748), and phlogopite (JCPDS card no. 01-085-2271). Phlogopite is the remaining phase after the dehydration of vermiculite and hydrobiotite [28]. The presence of forsterite (Mg_2SiO_4) and leucite ($KAlSi_2O_6$) agree well with the phase analysis on single vermiculite flakes and commercial vermiculite above 800 °C [19].

3.2. Porosity of FA and FA/Clay Ceramics

All ceramic cubes, instead of FA/Ka and FA/Vb, showed uniform macropore-size distribution with macropore diameters above 230 nm (Figure 3). In general, the macropore size of individual solids increased as follows: FA/Mk (234 nm) < FA/Va (548 nm) < FA/Kb (755 nm) = Fa/Ka (754 and 4070 nm) < FA/Vb (943 and 4070 nm) < FA

(1160 nm). FA/Ka and FA/Vb were characterized by bidisperse macropore-size distribution. Moreover, FA/Vb showed broad macropore-size distribution of smaller macropores with a maximum at 943 nm. The porosity was in the range between 28% and 46%.

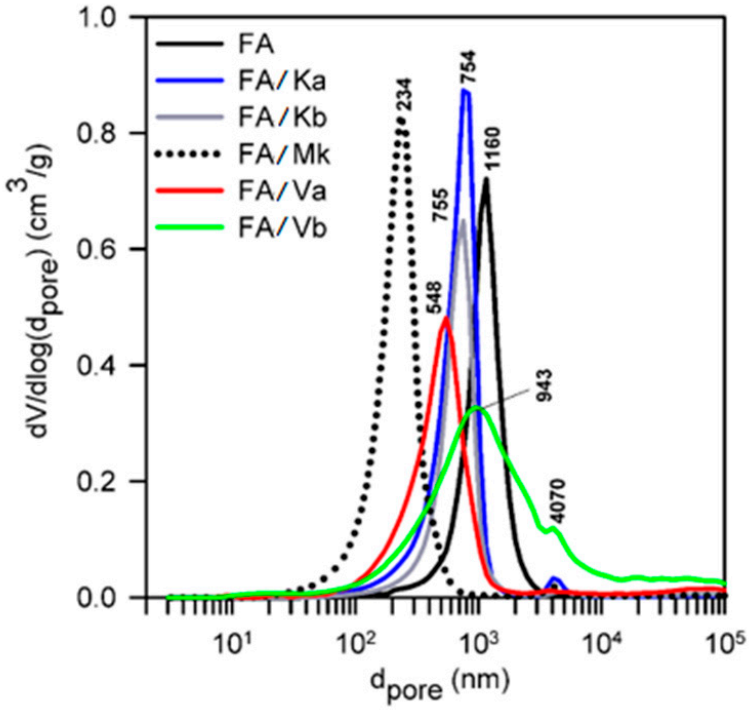


Figure 3. Mesopore- and macropore-size distributions of the investigated solids determined from high-pressure mercury porosimetry.

The results from nitrogen physisorption measurements (Figure 4) indicated that FA, FA/Ka, and FA/Kb (Figure 4a) in comparison with FA/Mk, FA/Va, and FA/Vb (Figure 4b) showed very low surface areas of 0.79, 1.26, and 1.07 m^2/g, respectively (Table 2), originating from macropores (Figure 4c). Additional smaller macropores from 80 to 200 nm were determined only in FA/Mk, FA/Va, and FA/Vb (Figure 4d). Therefore, FA/Mk, FA/Va, and FA/Vb ceramic samples had higher surface areas of 5.16, 2.09, and 2.30 m^2/g, respectively, as well as higher net pore volumes of 17.77, 6.34, and 10 cm^3 (STP)/g, respectively (Table 2). From the measured nitrogen isotherm (Figure 4b) and evaluated macropore-size distribution (Figure 4d), it is evident that FA/Vb possessed some macropores of 100 nm diameter not differentiated by high-pressure mercury porosimetry.

3.3. Thermal Transformation of Clays and FA/Clay Mixtures

The results of thermal changes in FA, clay samples, and FA/clay mixtures was obtained from thermogravimetry and derivate thermogravimetry (Table 3, Figure 5). Mass loss percentages obtained from TG curves and temperatures at maximum mass loss rate (T_m) obtained from derivative TG curves (Figure 5a) characterized the thermal decomposition steps of the studied samples (Table 3). Total mass loss percentages (Δm) were comparable to the L.O.I. value shown in Table 1, within a error of up to 2%.

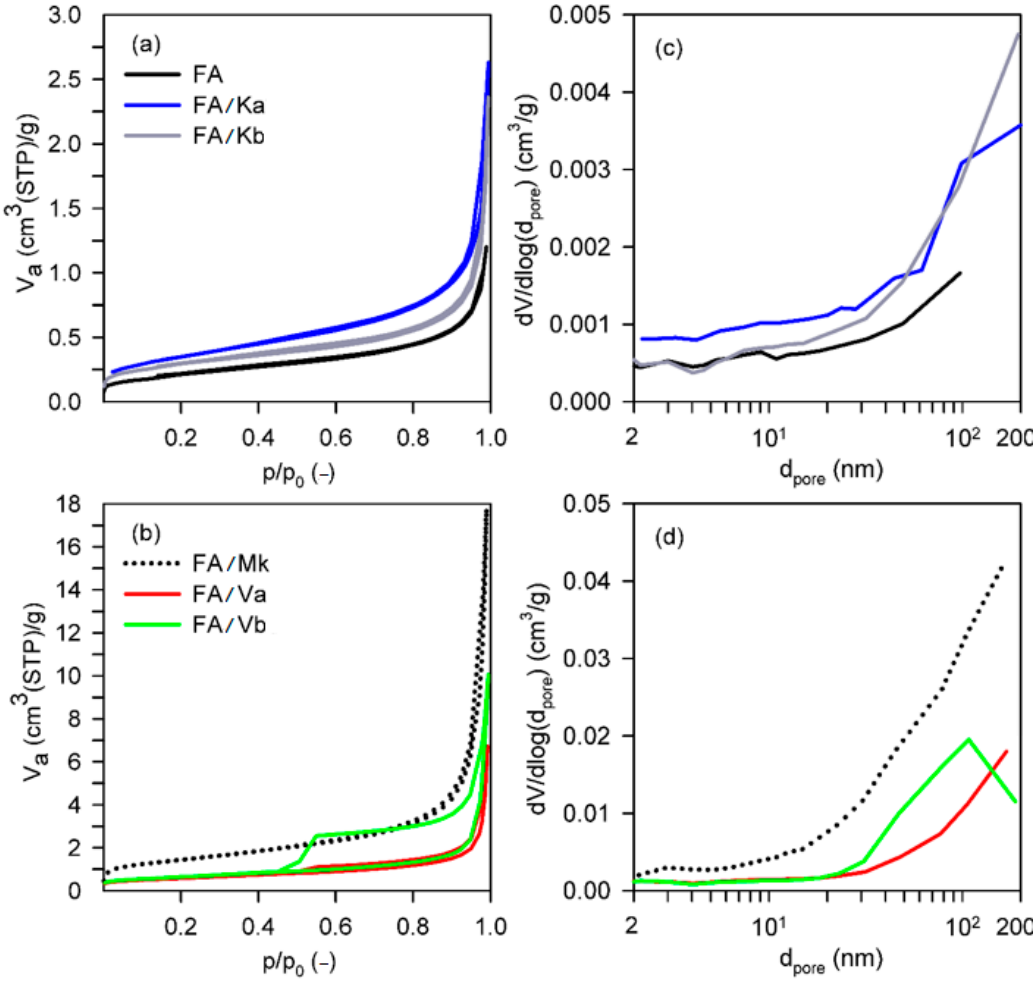


Figure 4. (**a**,**b**) Nitrogen adsorption–desorption isotherms at 77 K; (**c**,**d**) evaluated mesopore- and macropore-size distributions of the investigated solids from physisorption.

Table 2. Textural properties determined by high-pressure mercury porosimetry, helium pycnometry, and nitrogen physisorption at 77 K.

Sample	Hg Porosimetry and He Pycnometry				Physisorption	
	V_{intr} (cm^3/g)	ρ_{Hg} (g/cm^3)	ρ_{He} (g/cm^3)	ε (%)	S_{BET} (m^2/g)	V_{net} (cm^3(STP)/g)
FA	0.23	1.49	2.67	44	0.79	1.20
FA/Ka	0.28	1.43	2.27	37	1.26	2.63
FA/Kb	0.20	1.67	2.33	28	1.07	2.36
FA/Mk	0.31	1.40	2.40	42	5.16	17.77
FA/Va	0.24	1.64	2.59	37	2.09	6.73
FA/Vb	0.35	1.41	2.60	46	2.30	10.05

V_{intr}: specific intrusion volume determined from high-pressure mercury porosimetry. ρ_{Hg}: apparent (mercury) density determined from high-pressure mercury porosimetry. ρ_{He}: skeletal (true) density determined from helium pycnometry. ε: porosity determined by following calculation: ε (%) = $(1 - (\rho_{Hg}/\rho_{He})) \times 100$. S_{BET}: specific surface area determined from nitrogen physisorption at 77 K. V_{net}: net pore volume determined from nitrogen physisorption at 77 K.

Table 3. Thermal characteristics of FA, clays, and FA/clay mixtures.

Sample	Δm (%)	$T_{m\,1}$ (°C)	$T_{m\,2}$ (°C)	$T_{m\,3}$ (°C)	$T_{m\,4}$ (°C)	$T_{m\,5}$ (°C)	$T_{m\,6}$ (°C)	$T_{m\,7}$ (°C)	T_{1exo} (°C)	T_{2exo} (°C)
FA	−5.5	119	–	–	589	679	–	–	813	1025
Ka	−11.7	110	–	395	528	–	–	–		980
Kb	−11.2	108	–	326	519	–	–	–		975
Mk	−0.7	120	–	349	520	–	–	–		981
Va	−7.8	115	230	–	505	682	789	998		924
Vb	−10.9	112	217	–	501	658	827	989		857
FA/Ka	−12.1	104	–	361	532	–	866	–		966
FA/Kb	−10.8	102	–	344	510	–	840	–		954
FA/Mk	−4.3	112	–	–	538	699	845	–		978
FA/Va	−9.3	110	219	–	512	689	822	991	743	833
FA/Vb	−8.8	107	216	–	491	637	815	963	730	821

Δm: mass loss percentages obtained from TG curves and temperature intervals at maximum mass loss rate. T_m: mass loss rate from DTG curves. T_1 and T_2: temperatures of exotherm peak maxima from DTA curves.

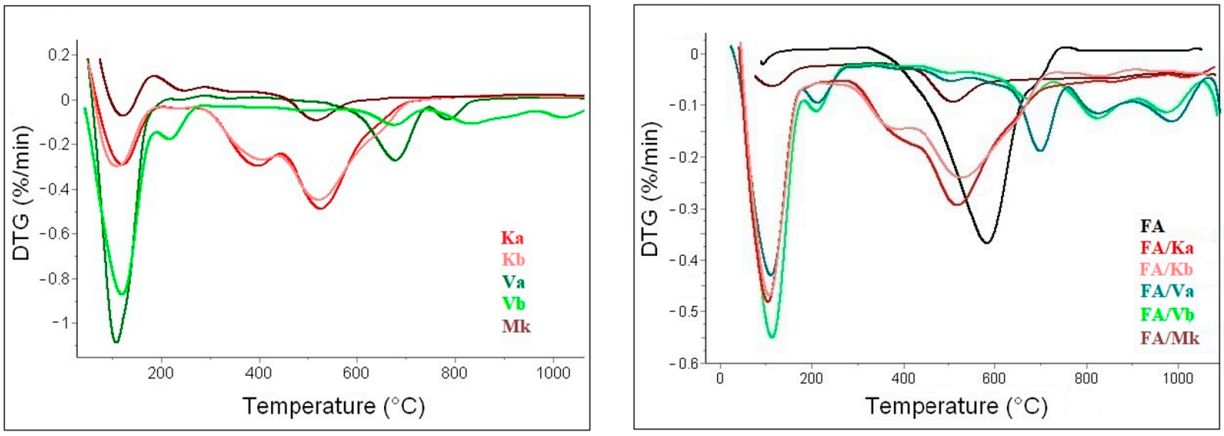


Figure 5. DTG curves of (**a**) kaolins and vermiculites; (**b**) FA and FA–clay mixtures.

Kaolinite transforms at temperatures below 1000 °C during the removal of water and hydroxyl groups directly into mullite and, therefore, kaolinite is classified as a mullite precursor of type I [30]. The DTG or DTA peak, which reflects the dehydroxylation of kaolinite, displays some variability of the formation of disordered metakaolinite and mullite. Kaolins Ka and Kb, as well as metakaolin (Mk), were dehydrated at a low temperature interval of up to 150 °C. Dehydroxylation of kaolinite and transformation to metakaolinite occurred at the temperature interval of 350–600 °C, and exothermic transformation of metakaolinite to mullite at about 980 °C (Table 3).

Mass loss of raw vermiculites during firing is a result of dehydration and dehydroxylation of vermiculite (Vm) and hydrobiotite (Hb). The three thermal mass losses are generally observed [13] (Table 3). The first loss is caused by the removal of physically adsorbed water as well as the first hydration sphere of interlayer cations up to 150 °C, the second mass loss of remaining bound water is associated with interlayer cations in the range of 180 to 250 °C, and the third mass loss and heat effects observed in the temperature range of 650 to 950 °C is due to the dehydroxylation of vermiculite. The dehydroxylation of raw Va takes place in the Hb > Vm mixed layer structure and was recorded on DTG curves of two different intensive endothermal maxima at 682 °C and at 789 °C. Similarly, raw Vb dehydroxylation of the Vm > Hb mixed layer structure produced two similar less intensive endo peaks at 658 and 827 °C (Figure 5a, Table 3). The exotherm maxima at 924 and 857 °C in Va and Vb, respectively, confirmed about a 67 °C higher temperature of forsterite crystallization from Hb > Vm than from Vm > Hb. Thermodynamic calculations on similar vermiculites

suggests that forsterite can exist with leucite and hematite in potassium aluminosilicate melt at 970 °C [18]. Enstatite was not found in the XRD patterns, but leucite ($KAlSi_2O_6$) was formed instead [19].

It is obvious that magnesium silicates in FA/Va and FA/Vb mixtures undergo transformation to different crystalline phase states at lower temperatures than pure FA, Va, and Vb (Table 3, Figure 5b). Exothermal maxima at 743 °C in FA/Va and 730 °C in FA/Vb were assigned to the crystallization of forsterite [31]. The XRD phase analysis of forsterite-based bricks FA/Va and FA/Vb confirmed the presence of crystalline forsterite (Mg_2SiO_4), diopside ($CaMgSi_2O_6$), leucite ($KAlSi_2O_6$), and phlogopite ($KMg_3AlSi_3O_{10}$) (Figure 2b). Crystallization of phases can be observed on the exotherm maxima at 924 and 857 °C in Va and Vb, respectively, as well as the maxima that dropped to 833 and 821 °C in FA/Va and FA/Vb, respectively. Enstatite ($MgSiO_3$) and forsterite crystallizing from 743 °C to 833 °C in FA/Va and from 730 °C to 821 °C in FA/Vb was already documented in literature [31–33].

3.4. Test Results of Ceramic Brick Cubes

3.4.1. Physical and Mechanical Properties

Progress in research on the thermal properties of clay minerals in fired bricks summarize the thermal mass loss, thermal phase transition, thermal expansion, and shrinkage [28]. Dimensional changes of kaolinite due to structural transformations between 25 and 1000 °C were described in the temperature sequences as follows: (1) below 150 °C, the loss of the adsorbed water caused only a minor contraction of about 0.05%; (2) lattice expansion in the temperature range from 470 to 550 °C was associated with a linear thermal expansion of 0.2%–0.3%; (3) dehydroxylation in the temperature range from 500 to 650 °C caused the first rapid shrinkage (1.0%–1.8%), and in the temperature range from 650 to 900 °C caused continuing shrinkage (1.5%–2.3%); (3) transformation of metakaolin to mullite between about 900 and 1000 °C was observed on the second rapid shrinkage (1.0%–3.7%).

The thermal shrinkage of vermiculite was evaluated at two stages [25]. The first thermal shrinkage occurred due to the dehydroxylation and crystallization of enstatite at about 750–910 °C. The second shrinkage was ascribed to the melting of vermiculite and liquid phase formation at a temperature higher than 910 °C.

CS values of the clay bricks were reported from 3.5 to 35 MPa, as well as a 5 MPa minimal value [34,35].

Mass loss (WL), drying shrinkage (DS), firing shrinkage (FS), and compressive strength (CS) values of FA and FA/clay ceramic bricks are provided in Table 4. The WL values (calculated from Equation (1)) corresponded to the TG mass loss Δm (%) (Table 3). The DS value (calculated from Equation (2)) was from 0.6% for FA to 6.3% for FA/Va. FS values (calculated from Equation (3)) were below 8%, except of FA (8.8%) and FA/Kb (9.5%), and they met the requirements for the category of good-quality bricks [27]. CS values of FA and FA/clay ceramic bricks from 9.1 to 25.5 MPa were in the range of the clay bricks [34,35].

Table 4. Physical and mechanical properties of FA and FA/clay ceramic bricks.

Sample	WL (%)	DS (%)	FS (%)	CS (MPa)
FA	4.71 ± 0.07	0.60 ± 0.16	8.81 ± 0.16	9.98 ± 0.48
FA/Ka	11.86 ± 0.12	1.80 ± 0.19	6.10 ± 0.19	14.97 ± 1.23
FA/Kb	11.59 ± 0.15	2.24 ± 0.15	9.46 ± 0.14	25.57 ± 5.53
FA/Mk	9.90 ± 0.10	3.04 ± 0.14	2.86 ± 0.18	9.11 ± 0.93
FA/Va	10.13 ± 0.08	6.27 ± 0.17	6.75 ± 0.16	14.05 ± 3.61
FA/Vb	9.25 ± 0.07	3.73 ± 0.29	2.50 ± 0.30	12.25 ± 5.88

WL: mass loss at 1000 °C (1). DS: drying shrinkage at 105 °C (2). FS: firing shrinkage at 1000 °C (3). CS: compressive strength, MPa.

The influence of clay minerals on the mechanical strength of the fired bricks and on porosity is commonly positively correlated. In most cases, an increased amount of

clay minerals in brick-making raw material at the expense of non-clay phases improves mechanical strength [28]. Potassium and sodium alkali metal elements (which are mostly bound in the structures of micas and feldspars) act as fusing agents on the reactivity of silica and alumina, and they support the decrease in the firing temperature, high shrinkage, and low porosity [36]. In this work, mullite exotherm in mullite-based ceramic of FA at about 1025 °C was in FA/Ka, FA/Mk, and FA/Kb reduced by 59 °C and 71 °C. The decrease in temperatures and the difference between FA/Ka and FA/Kb can be explained by the presence of muscovite 4 and 7 mass% in kaolins Ka and Kb, respectively (% calculated in the previous work [26]). Compared to mullite-based ceramics, the mixtures FA/Va and FA/Vb were fired to the forsterite-diopside-based ceramics at temperatures lower by 192 °C and 204 °C, respectively.

The effect of alkali on high shrinkage, low porosity, and low compressive strength (Figure 6) was evidenced according to (1) the positive correlation between the FS and K_2O/SiO_2 mass ratio (Figure 6a), (2) the negative correlation between FS and porosity (Figure 6b), and (3) the negative correlation between CS and porosity (Figure 6c).

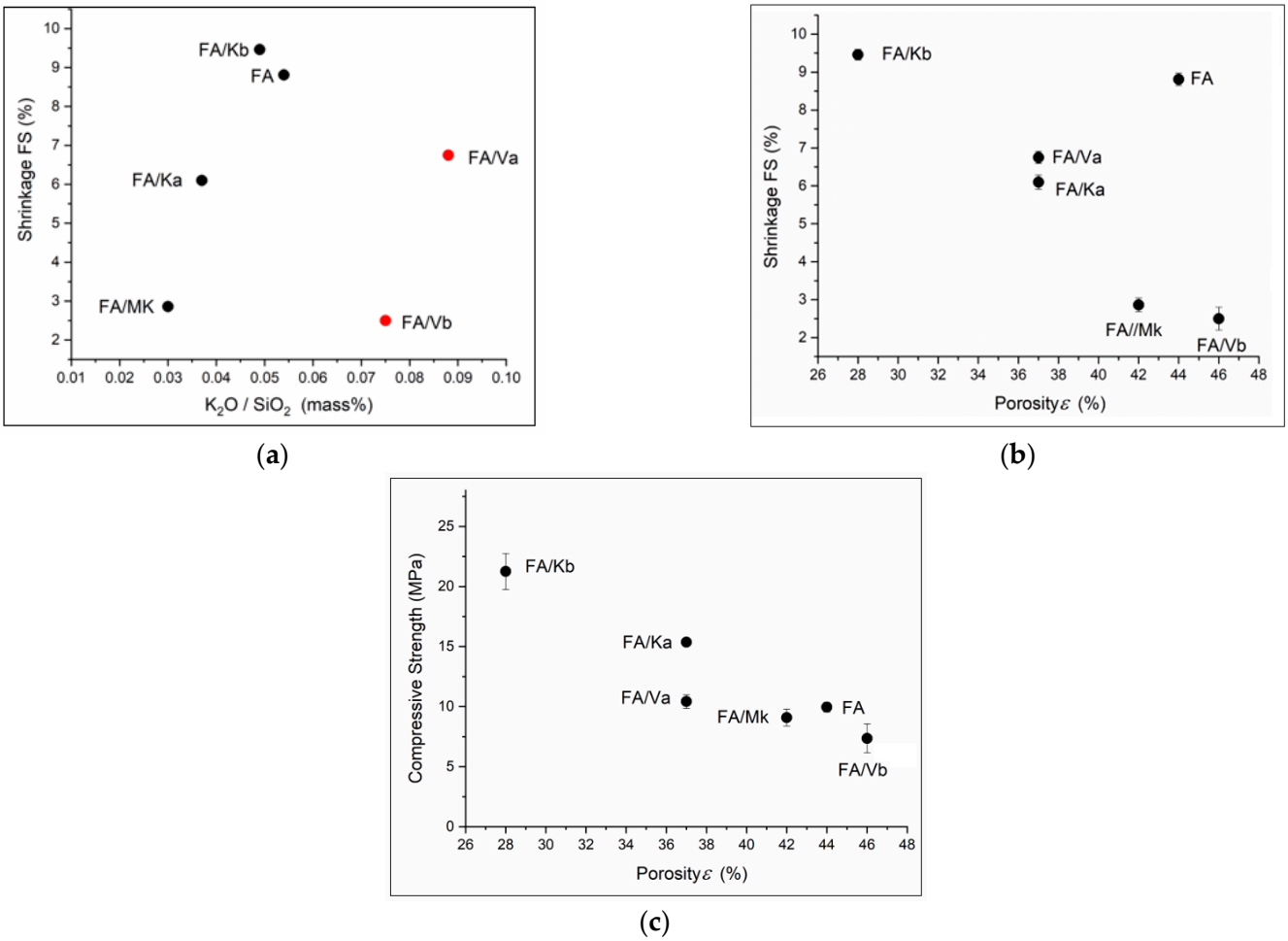


Figure 6. Mullite-based FA/kaolins and forsterite-based FA/vermiculites brick relations between (**a**) FS to the f K_2O/SiO_2 mass ratio; (**b**) FS to the porosity; and (**c**) CS to the porosity.

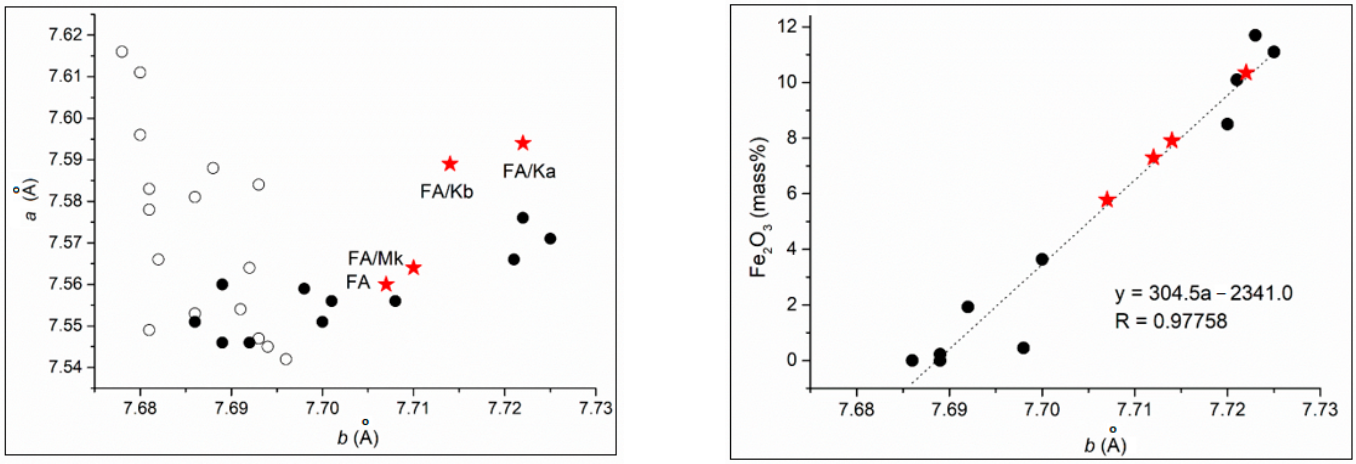
The FS of mullite-based bricks decreased in the descending order of FA/Kb < FA/Ka < FA/Mk due to the decreasing presence of the alkali muscovite (Figure 6a), while the formation of mullite (temperature at T_{2exo}, shown in Table 3) was in the ascending order of 954 °C, 966 °C, and 978 °C, respectively. The FS of forsterite-based bricks FA/Va 6.75% in comparison with FA/Vb 2.5% correlated with the total mass losses of 9.3% and 8.8%,

respectively, resulting from the dehydration and dehydroxylation of vermiculite and the crystallization of enstatite–diopside.

Crystallization of mullite was documented in many works. It is generally accepted that (1) crystallization of mullite starts after enough alkali atoms migrated from muscovite/illite to its surrounding low alkali matrix; (2) mullite crystals precipitating in muscovite/illite usually contain more Fe and are larger than that from kaolinite [37,38]; and (3) mullite lattice parameter *b* increases with the Fe_2O_3 content due to Fe(III) substituting for Al(III) [39,40]. It is very well known that mullite may crystallize at temperatures as low as about 900 °C. The formation of solid solutions between mullite and transition metal cations affects the thermal expansion of mullite through the distortion of the Al–O octahedra. The initially crystallized mullite phase is characterized by a low SiO_2 content, accompanied by a decrease in the *b*/*a* unit-cell parameter ratio to about 1, for which it is called pseudo-tetragonal mullite [41]. The Fe(III) cations enter into the mullite lattice at the first stage of mullite crystallization at about 900 °C [39]. Lattice parameters of mullites were calculated (Table 5) and were plotted into the *a*, *b* relation along with the pure mullites and mullites with Fe(III) published in [39] (Figure 7a).

Table 5. Lattice parameters of mullites and calculated percentages Fe_2O_3 using Equation (4).

Sample	*a* (Å)	*b* (Å)	*c* (Å)	Fe_2O_3 (mass%)
FA	7.560	7.707	2.887	5.78
FA/Ka	7.594	7.722	2.889	10.35
FA/Kb	7.589	7.714	2.889	7.91
FA/Mk	7.564	7.712	2.892	7.30



(**a**) (**b**)

Figure 7. Mullite-based ceramic bricks: (**a**) lattice parameters *a*, *b* of mullites (o); mullites with substitution Fe (•) published in [39]; and in FA/kaolin bricks (★). (**b**) Relation in lattice of mullites between substituted Fe_2O_3 mass% and parameter *b* (•) published in [39] and calculated according to Equation (4) in FA/Kaolin bricks (★).

Fe_2O_3 mass% in the lattice of mullites and parameter *b* values according to Dong [39] showed a positive relationship (Figure 7b), which can be supported by Equation (4):

$$Fe_2O_3\ (\text{mass\%}) = 304.5b - 2341.0 \quad (4)$$

The amount of Fe_2O_3 in the lattice of mullites in the ceramic bricks calculated according to Equation (4) was in the range from 5.78 mass% in FA to 10.35 mass% in FA/Ka (Table 5), and they are plotted in Figure 7b.

3.4.2. Photocatalytic Activity Test of Ceramic Bricks

The products obtained from the photocatalytic decomposition of the methanol–water mixture in the presence of all ceramic bricks are compared in Figure 8. Mullite-based FA bricks produced the lowest hydrogen yield of 116 µmol/g_{cat} (Figure 8a), corresponding to the lowest Fe_2O_3 5.6% substitution in mullite (Figure 8b). The hydrogen yield of 320 µmol/g_{cat} produced by mullite-based FA/Ka bricks reflexed higher Fe_2O_3 10.4% lattice substitution in mullite, which can be supported by the bidisperse macropore-size distribution (see Section 3.2).

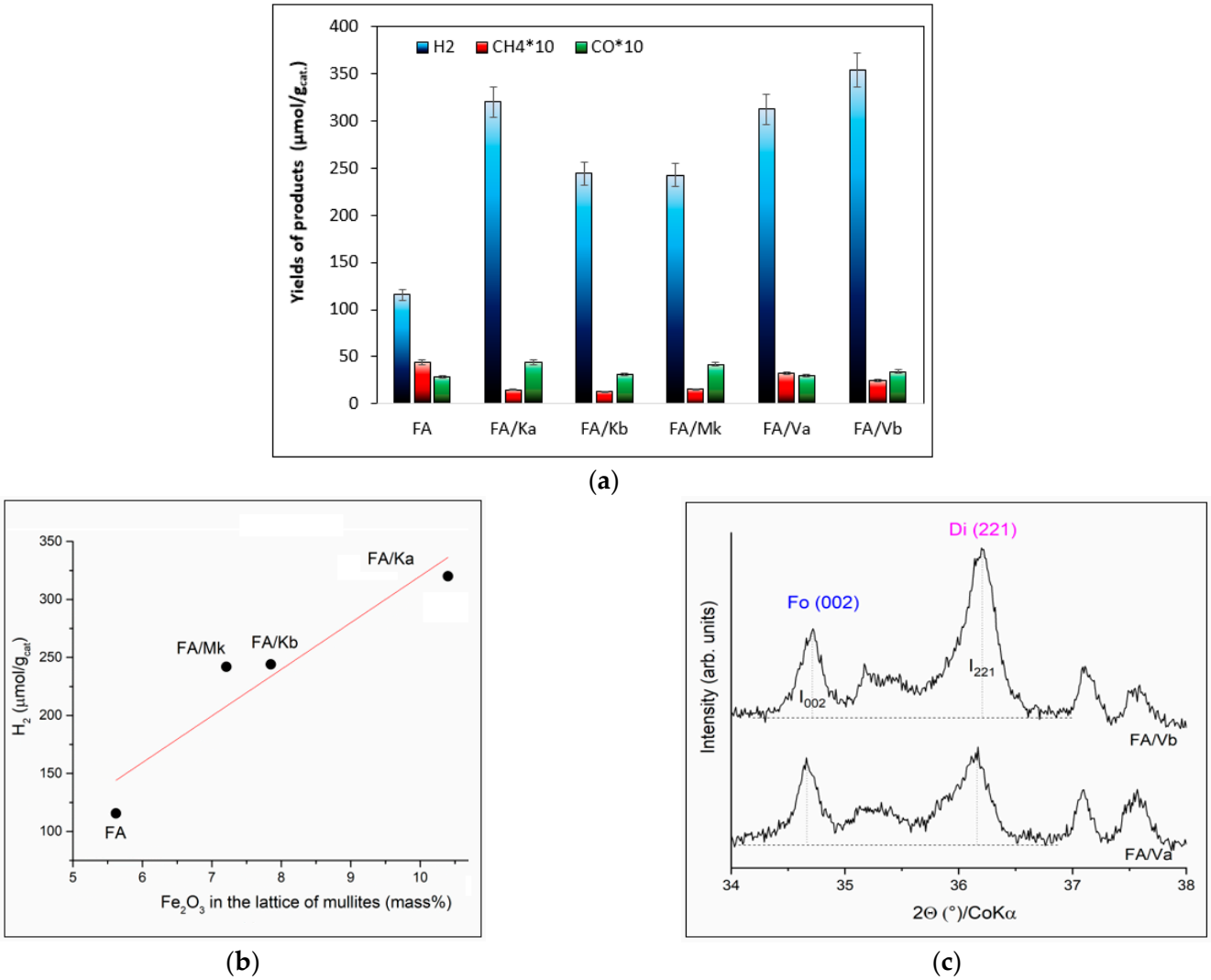


Figure 8. Photocatalytic decomposition of methanol: (**a**) Yields of all obtained products from the photocatalytic decomposition of methanol in the presence of the investigated ceramic bricks after 4 h of 254 nm irradiation (*multiplied by 10). (**b**) Relation between the yield of hydrogen and Fe_2O_3 percentages in the lattice of mullites calculated using Equation (4). (**c**) XRD pattern segment with position and intensity peaks 002 of Fo and 221 of Di in forsterite-based FA/Va and FA/Vb bricks.

XRD patterns of forsterite-based FA/Va and FA/Vb ceramics (Figure 2b) draw attention to the different intensities (I) of diffractions of forsterite, Fo ($2MgO{\cdot}SiO_2$), and diopside, Di ($CaO{\cdot}MgO{\cdot}2SiO_2$). As shown in Figure 8c, the peak intensity of Fo (I_{002}) and Di (I_{221}) were 0.53 for FA/Va and 0.86 for FA/Vb, which may indicate about the same amount of Fo and Di in FA/Va and a predominance of Di over Fo in FA/Vb. Although Fo and Di may contain substituted Fe, it has been declared that CaO nanoparticles of Di showed better catalytic activity than MgO nanoparticles of Fo [21]. As the bond strength of Ca–O was

lesser than Mg–O, it was able to produce active sites easily via the cleavage of the bond. Bidisperse macropore-size distributions in FA/Vb (see in Section 3.2) are significant in accommodation of larger CaO and smaller MgO nanoparticles and can explain the higher hydrogen yield of 354 $\mu mol/g_{cat}$ in the presence of Di in FA/Vb bricks in comparison with a lower yield of 312 $\mu mol/g_{cat}$ produced in the presence of FA/Va bricks.

4. Conclusions

The paper presents mullite- and forsterite-based ceramic bricks prepared using kaolin and vermiculites as precursors with fly ash mixtures.

Physical and mechanical properties of mullite-based and forsterite-based ceramic bricks were compared and discussed.

The thermal shrinkage of kaolin-based bricks was lowered by the presence of alkali muscovite. The thermal shrinkage of forsterite-based bricks was relative to the total mass loss due to dehydration and dehydroxylation of vermiculite–hydrobiotite mixed layers and the crystallization of enstatite–forsterite–diopside. The thermal shrinkage and compressive strength of mullite-based and forsterite-based ceramics were in the range of good-quality clay bricks.

Different photocatalytic generations of hydrogen in the presence of mullite-based ceramic bricks and forsterite-based ceramic bricks was positively correlated with the percentages of Fe_2O_3 in the lattice of mullites and to the predominance of diopside over forsterite in forsterite-based ceramic bricks.

Author Contributions: Conceptualization, M.V.; methodology, M.V.; validation, M.F.E. and E.P.; formal analysis, M.V., L.M. and M.F.E.; investigation, V.B., K.S. and L.M.; resources, V.B.; data curation, V.B.; writing—original draft preparation, M.V.; writing—review and editing, M.V.; visualization, M.V., L.M. and E.P.; supervision, M.V.; project administration, M.V.; funding acquisition, M.V. All authors have read and agreed to the published version of the manuscript.

Funding: This research was funded by the Large Research Infrastructure ENREGAT (project no. LM2023056).

Data Availability Statement: Not applicable.

Acknowledgments: The authors thank Alexandr Martaus for XRD and XRF analyses.

Conflicts of Interest: The authors declare no conflict of interest.

References

1. Ahmaruzzaman, M. A review on the utilization of fly ash. *Prog. Energ. Combust.* **2010**, *36*, 327–363. [CrossRef]
2. Cultrone, G.; Rosua, F.J.C. Growth of metastable phases during brick firing: Mineralogical and microtextural changes induced by the composition of the raw material and the presence of additives. *Appl. Clay Sci.* **2020**, *185*, 105419. [CrossRef]
3. Sun, Z.; Zhou, H.; Jiang, H.H.; Zhang, W.Y.; Mao, L.Q. Recycling municipal solid waste incineration fly ash in fired bricks: An evaluation of physical-mechanical and environmental properties. *Construct. Build. Mater.* **2021**, *294*, 1234765. [CrossRef]
4. Linglin, X.; Wei, G.; Tao, W.; Nanru, Y. Study on fired bricks with replacing clay by fly ash in high volume ratio. *Constr. Build. Mater.* **2005**, *19*, 243–247. [CrossRef]
5. Húlan, T.; Trník, A.; Kaljuvee, T.; Uibu, M.; Štubňa, I.; Kallavus, U.; Traksmaa, R. The study of firing of a ceramic body made from illite and fluidized bed combustion fly ash. *J. Therm. Anal. Calorim.* **2017**, *127*, 79–89. [CrossRef]
6. Murmu, A.L.; Patel, A. Towards sustainable bricks production: An overview. *Constr. Build. Mater.* **2018**, *165*, 112–125. [CrossRef]
7. Muñoz Velasco, P.; Morales Ortíz, M.P.; Mendívil Giró, M.A.; Muńoz Velasco, L. Fired clay bricks manufactured by adding wastes as sustainable construction material – A review. *Constr. Build. Mater.* **2014**, *63*, 97–107. [CrossRef]
8. Queralt, I.; Querol, X.; Soler, A.L.; Plans, F. Use of coal fly ash for ceramics: A case study for a large Spanish power station. *Fuel* **1997**, *76*, 787–791. [CrossRef]
9. Chen, S.; Cai, W.H.; Wu, J.M.; Ma, Y.X.; Li, C.H.; Shi, Y.S.; Yan, C.Z.; Wang, Y.J.; Zhang, H.X. Porous mullite ceramics with a fully closed-cell structure fabricated by direct coagulation casting using fly ash hollow spheres/kaolin suspension. *Ceram. Int.* **2020**, *46*, 17508–17513. [CrossRef]
10. Aripin, H.; Mitsudo, S.; Prima, E.S.; Sudiana, I.N.; Kikuchi, H.; Sano, S.; Sabchevski, S. Crystalline mullite formation from mixtures of alumina and a novel material–Silica xerogel converted from sago waste ash. *Ceram. Int.* **2015**, *41*, 6488–6497. [CrossRef]
11. Harbi, R.; Derabla, R.; Nafa, Z. Improvement of the properties of a mortar with 5% of kaolin fillers in sand combined with metakaolin, brick waste and glass powder in cement. *Constr. Build. Mater.* **2017**, *152*, 632–641. [CrossRef]

12. Sutcu, M. Influence of expanded vermiculite on physical properties and thermal conductivity of clay bricks. *Ceram. Int.* **2015**, *41*, 2819–2827. [CrossRef]
13. Wang, S.; Gainey, L.; Wang, X.D.; Marinelli, J.; Deer, B.; Wang, X.; Mackinnon, I.D.R.; Xi, Y. Effects of vermiculite on in-situ thermal behaviour, microstructure, physical and mechanical properties of fired clay bricks. *Constr. Build. Mater.* **2022**, *316*, 125828. [CrossRef]
14. Marcos, C.; Argűelles, A.; Ruíz-Conde, A.; Sánchez-Soto, P.J.; Blanco, J.A. Study of the dehydration process of vermiculites by applying a vacuum pressure: Formation of interstratified phases. *Mineral. Mag.* **2003**, *67*, 1253–1268. [CrossRef]
15. Kikuchi, R.; Kogure, T. Structural and compositional variances in 'hidrobiotite' sample from Palabora, South Africa. *Clay Sci.* **2018**, *22*, 39–52.
16. Ramírez-Valle, V.; De Haro, M.C.J.; Avilés, M.A.; Pérez-Maqueda, L.A.; Durán, A.; Pascual, J.; Pérez-Rodríguez, J.L. Effect of interlayer cations on high-temperature phases of vermiculite. *J. Therm. Anal. Calorim.* **2006**, *84*, 147–155. [CrossRef]
17. Suquet, H.; Mallard, C.; Quarton, M.; Dubernat, J.; Pezerat, H. Etude du biopyribole formé par chauffage des vermiculites magnésiennes. *Clay Miner.* **1984**, *19*, 217–227. [CrossRef]
18. Luneng, R.; Bertel, S.N.; Mikkelsen, J.; Ratvik, A.P.; Grande, T. Chemical durability of thermal insulating materials in hall-héroult electrolysis cells. *Ceramics* **2019**, *2*, 441–459. [CrossRef]
19. Petersen, R.R.; Christensen, F.S.; Jørgensen, N.T.; Gustafson, S.; Lindbjerg, L.A.; Yue, Y. Preparation and thermal properties of commercial vermiculite bonded with potassium silicate. *Termochim. Acta* **2021**, *699*, 178926. [CrossRef]
20. Son, B.T.; Long, N.V.; Hang, N.T.N. Fly-ash, foundry sand-, clay- and pumice-based metal oxide nanocomposites as green photocatalysts. *RSC Adv.* **2021**, *11*, 30805. [CrossRef]
21. Venkatraman, K.S.; Saraswat, M.; Choudhary, R.; Senatov, F.; Kaloshkin, S.; Swamiappan, S. Photocatalytic degradation of methylene blue dye by calcium-and magnesium-based silicate ceramics. *ChemistrySelect* **2020**, *5*, 12198–12205. [CrossRef]
22. Venkatraman, K.S.; Vijayakumar, N.; Bal, D.K.; Mishra, A.; Gupta, B.; Mishra, V.; Wysokowski, M.; Koppala, S.; Swamiappan, S. Degradation of environmentally harmful textile dye rhodamine B using silicate ceramic photocatalysts. *Inorg. Chem. Commun.* **2022**, *142*, 109674. [CrossRef]
23. *ASTM C326-09*; Standard Test Method for Drying and Firing Shrinkage of Ceramic Whiteware Clays. ASTM International: West Conshohocken, PA 19428-2959, USA, 2018.
24. Standard Specification for Coal Fly Ash and Raw or Calcined Natural Pozzolan for Use as a Mineral in Concrete. ASTM International: West Conshohocken, PA, USA, 2019.
25. Wang, S.; Gainey, L.; Wang, X.D.; Mackinnon, I.D.R.; Xi, Y.F. Influence of palygorskite on in-situ thermal behaviours of clay mixtures and properties of fired bricks. *Appl Clay Sci.* **2022**, *216*, 106384. [CrossRef]
26. Valášková, M.; Klika, Z.; Novosad, B.; Smetana, B. Crystallization and quantification of crystalline and non-crystalline phases in kaolin-based cordierites. *Materials* **2019**, *12*, 3104. [CrossRef]
27. Valášková, M.; Madejová, J.; Inayat, A.; Matějová, L.; Ritz, M.; Martaus, A.; Leštinský, P. Vermiculites from Brazil and Palabora: Structural changes upon heat treatment and influence on the depolymerization of polystyrene. *Appl. Clay Sci.* **2020**, *192*, 105639. [CrossRef]
28. Wang, S.; Gainey, L.; Mackinnon, I.D.R.; Allen, C.; Gu, Y.; Xi, Y. Thermal behaviors of clay minerals as key components and additives for fired brick properties: A review. *J. Build. Eng.* **2023**, *66*, 105802. [CrossRef]
29. Warr, L.N. IMA–CNMNC approved mineral symbols. *Mineral. Mag.* **2021**, *85*, 291–320. [CrossRef]
30. Schneider, H.; Komarneni, S. (Eds.) *Mullite*; Wiley VCH: Weinheim, Germany, 2005.
31. Tsai, M.T. Effects of hydrolysis processing on the characterization of forsterite gel fibers: II, crystallites and microstructural evolutions. *J. Eur. Ceram. Soc.* **2002**, *22*, 1085–1094. [CrossRef]
32. Pérez-Maqueda, L.A.; Balek, V.; Poyato, J.; Pérez-Rodríquez, J.L.; Šubrt, J.; Bountsewa, I.M.; Beckman, I.N.; Málek, Z. Study of natural and ion exchanged vermiculite by emanation thermal analysis, TG, DTA and XRD. *J. Therm. Anal. Calor.* **2003**, *71*, 715–726. [CrossRef]
33. Ma, L.Y.; Su, X.L.; Xi, Y.F.; Wei, J.M.; Liang, X.L.; Zhu, J.X.; He, H.P. The structural change of vermiculite during dehydration processes: A real-time in-situ XRD method. *Appl. Clay Sci.* **2019**, *183*, 10533. [CrossRef]
34. Velasco, P.M.; Ortiz, M.P.M.; Giró, M.A.M.; Melia, D.M.; Rehbein, J.H. Development of sustainable fired clay bricks by adding kindling from vine shoot: Study of thermal and mechanical properties. *Appl. Clay Sci.* **2015**, *107*, 156–164. [CrossRef]
35. Hulan, T.; Stubna, I.; Ondruska, J. The influence of fly ash on mechanical properties of clay-based ceramics. *Minerals* **2020**, *10*, 930. [CrossRef]
36. Moreno-Tovar, R.; Pérez-Moreno, F.; Arenas-Flores, A.; Romero-Guerrero, L.M. Thermal behavior, chemical, mineralogical and optical characterization of clays (kaolin) for industrial use as refractory material. *Adv. Mater. Res.* **2014**, *976*, 174–178. [CrossRef]
37. Schneider, H.; Rager, H. Iron incorporation in mullite. *Ceram. Int.* **1986**, *12*, 117–125. [CrossRef]
38. Lecomte, G.L.; Bonnet, J.P.; Blanchart, P. A study of the influence of muscovite on the thermal transformations of kaolinite from room temperature up to 1100 °C. *J. Mater. Sci.* **2007**, *42*, 8745–8752. [CrossRef]
39. Dong, Y.; Feng, X.; Feng, X.; Ding, Y.; Liu, X.; Meng, G. Preparation of low-cost mullite ceramics from natural bauxite and industrial waste fly ash. *J. Alloys Compd.* **2008**, *460*, 599–606. [CrossRef]

40. Valášková, M.; Blahůšková, V.; Vlček, J. Effects of kaolin additives in fly ash on sintering and properties of mullite ceramics. *Minerals* **2021**, *11*, 887. [CrossRef]
41. Okada, K.; Otsuka, N.; Somiya, S. Review of mullite synthesis routes in Japan. *Am. Ceram. Soc. Bull.* **1991**, *70*, 1633–1640.

Disclaimer/Publisher's Note: The statements, opinions and data contained in all publications are solely those of the individual author(s) and contributor(s) and not of MDPI and/or the editor(s). MDPI and/or the editor(s) disclaim responsibility for any injury to people or property resulting from any ideas, methods, instructions or products referred to in the content.